

Quasi-three-dimensional hydrodynamics of the corona region of laser irradiation of a slab

Xiao-Mei Dong(董晓梅), Ben-Jin Guan(关本金), and Ying-Jun Li(李英骏)
Citation: Chin. Phys. B, 2024, 33 (**8**): 085203. DOI: 10.1088/1674-1056/ad4532

What follows is a list of articles you may be interested in

Power transfer efficiency in an air-breathing radio frequency ion thruster

Gao-Huang Huang(黄高煌), Hong Li(李宏), Fei Gao(高飞), and You-Nian Wang(王友年)
Chin. Phys. B, 2024, 33 (**7**): 075201. DOI: 10.1088/1674-1056/ad426c

Velocity analysis of supersonic jet flow in double-cone ignition scheme

Zhong-Yuan Zhu(朱仲源), Cheng-Long Zhang(张成龙), and Ying-Jun Li(李英骏)
Chin. Phys. B, 2024, 33 (**6**): 065203. DOI: 10.1088/1674-1056/acc1d4

Global dust density in two-dimensional complex plasma

Yi-Zhen Zhao(赵逸真), Song-Fen Liu(刘松芬), Wei Kong(孔伟), and Fang Yang(杨芳)
Chin. Phys. B, 2024, 33 (**6**): 065201. DOI: 10.1088/1674-1056/ad2a76

Diagnosing ratio of electron density to collision frequency of plasma surrounding scaled model in a shock tube using low-frequency alternating magnetic field phase shift

Ming-Xing Wu(吴明兴), Kai Xie(谢楷), Yan Liu(刘艳), Han Xu(徐晗), Bao Zhang(张宝), and De-Yang Tian(田得阳)
Chin. Phys. B, 2024, 33 (**5**): 055204. DOI: 10.1088/1674-1056/ad2d56

Probing the peripheral self-generated magnetic field distribution in laser-plasma magnetic reconnection with Martin—Puplett interferometer polarimeter

Ya-Peng Zhang(张雅芃), Jia-Wen Yao(姚嘉文), Zheng-Dong Liu(刘正东), Zuo-Lin Ma(马作霖), and Jia-Yong Zhong(仲佳勇)
Chin. Phys. B, 2024, 33 (**4**): 045206. DOI: 10.1088/1674-1056/ad24db

---

Quasi-three-dimensional hydrodynamics of the corona region of laser irradiation of a slab

Xiao-Mei Dong(董晓梅), Ben-Jin Guan(关本金), and Ying-Jun Li(李英骏)†

State Key Laboratory for Tunnel Engineering, China University of Mining and Technology, Beijing 100083, *China*

(Received 27 February 2024; revised manuscript received 25 April 2024; accepted manuscript online 30 April 2024)

This paper introduces and establishes a quasi-three-dimensional physical model of the interaction between a laser and a slab target. In contrast to previous one-dimensional analytical models, this paper innovatively fits the real laser conditions based on an isothermal, homogeneous expansion similarity solution of the ideal hydrodynamic equations. Using this simple model, the evolution law and analytical formulae for key parameters (e.g., temperature, density and scale length) in the corona region under certain conditions are given. The analytical solutions agree well with the relevant results of computational hydrodynamics simulation. For constant laser irradiation, the analytical solutions provide a meaningful power-law scaling relationship. The model provides a set of mathematical and physical tools that give theoretical support for adjusting parameters in experiments.

Keywords: plasma, self-similarity method, fluid dynamics calculations

PACS: 52.38.–r, 47.85.Dh **DOI:** 10.1088/1674-1056/ad4532

1. Introduction

In recent years, the interaction between lasers and slab targets has been a focal point of research, playing a crucial role in reproducing research in cutting-edge fields such as laboratory astrophysics[1–9] and inertial confinement fusion (ICF).[10–20] As an indispensable research tool, the laser–target interaction method has aided the performance of related research in many fields. From both experimental and simulation aspects, whether it is the law of evolution of the electromagnetic field[1] or the change of the topological structure of magnetic reconnection,[2] the outflow of magnetic reconnection,[3] the loop-top x-ray source[4] and guiding field magnetic reconnection[5] realized using high-energy laser-driven slab targets in the laboratory, are all based on three-dimensional laser irradiation slab target experiments. In the field of ICF, there is an urgent need for three-dimensional analytical models for theoretical interpretation and support in studying the acceleration of super-hot electrons[10,11] and high-energy protons[12] produced by the interaction of laser pulses with slab targets. Despite extensive research there is a scarcity of published articles addressing theoretical analyses. Li and Cheng and colleagues have established one-dimensional and two-dimensional perturbation self-similar hydrodynamics models of slab targets under line focusing laser conditions to solve the above issues, giving a set of isothermal, uniformly expanding self-similar solutions.[21–23] However, there is a lack of relevant research reports on the physical analysis of three-dimensional point-focusing laser irradiation of slab targets to get closer to real experimental conditions.

This paper further improves and develops the self-similar model proposed by Li[21,22] in 2001 to establish a quasi-three-dimensional analytical model of laser–target interaction, revealing key physical parameters such as electron temperature, electron density and plasma length during this process. The results obtained through this model are very consistent with the trend of expensive and time-consuming numerical simulation results. Compared with previous complex and time-consuming numerical simulation methods in hydrodynamics and atomic dynamics, this analytical method[24–26] has the advantages of a clear process and rapid calculation. More importantly, it can reverse a set of required conditions back to the experimental parameters required to produce these conditions by laser–target interaction.

Based on the quasi-three-dimensional model of laser–target interaction established in this paper, and on the basis of matching with the numerical simulation results of previous researchers,[27] theoretical analysis is further given for some related experimental simulations using the analytical model formula. In addition, the establishment of this model is expected to provide more methods for use in related fields, such as the evolution of magnetic fields in laser–target interaction, the generation of magnetic reconnection in laboratory astrophysics, and to provide theoretical support for understanding plasma transport transitions[28] and related material processing.[29]

This paper is structured as follows. Section 2 presents the relevant assumptions of the model, obtains the self-similar equation and state equation and establishes a fluid mechanics model of plasma in the corona region. Section 3 gives the formula for analytical solution and related analysis of the model at different time stages. The final conclusions are given in Section 4.

†Corresponding author. E-mail: lyj@aphy.iphy.ac.cn

© 2024 Chinese Physical Society and IOP Publishing Ltd

2. Self-similar physical model building and formula derivation

2.1. Model building

A quasi-three-dimensional model of a point-focused laser interacting with a slab target in cylindrical coordinates is shown in Fig. 1. The laser is driven from the right side, and the interaction between the laser and the target heats and vaporizes it to produce plasma; the direction of expansion of the plasma is away from the target surface. The incident path of the laser forms a cylindrical path trajectory, but the actual region on the target surface is a focused circular spot. At a certain moment in the forward path of the laser, the angle formed with the target surface is θ.

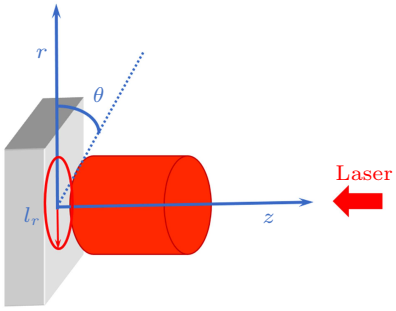


Fig. 1. Schematic diagram of the interaction between laser and target.

When a slab target is irradiated by a laser to produce plasma, the entire region is usually divided into three regions:[30,31] the compression region, the conduction region and the corona region. The corona region usually appears near the boundary of the plasma. In this region, due to the interaction between ions and electrons, the electric field strength changes greatly, resulting in a discontinuity of electron density. The corona region is usually considered as a non-uniform region in the plasma, and the main source of the magnetic field generated by the interaction between the laser and the target is the nonlinear electron density and temperature gradient in this region.[1] Therefore, the main region of interest in this paper is the corona region that leaves the target surface, and the electron density (n_e) is less than the critical density (n_c). This region is in a state of non-local thermodynamic equilibrium, and electrons and ions have their own temperatures, respectively reaching their Maxwell distribution. Considering that the mass of ions is much greater than that of electrons, a two-dimensional ideal fluid mechanics model is established with ions as the background

$$\frac{\partial \rho}{\partial t}+\frac{1}{r}\frac{\partial(\rho r v_r)}{\partial r}+\frac{\partial(\rho v_z)}{\partial z}+\frac{1}{r}\frac{\partial(\rho v_\theta)}{\partial \theta}=0, \tag{1}$$

$$\begin{cases}\rho\left(\dfrac{\partial v_r}{\partial t}+v_r\dfrac{\partial v_r}{\partial r}+\dfrac{v_\theta}{r}\dfrac{\partial v_r}{\partial \theta}+v_z\dfrac{\partial v_r}{\partial z}\right)+\dfrac{\partial p}{\partial r}=0,\\ \rho\left(\dfrac{\partial v_z}{\partial t}+v_r\dfrac{\partial v_z}{\partial r}+\dfrac{v_\theta}{r}\dfrac{\partial v_z}{\partial \theta}+v_z\dfrac{\partial v_z}{\partial z}\right)+\dfrac{\partial p}{\partial z}=0,\end{cases} \tag{2}$$

$$\begin{aligned}&\frac{\partial}{\partial t}\left[\rho\left(\varepsilon+\frac{v^2}{2}\right)\right]\\ &=-\frac{1}{r}\frac{\partial\left[\rho v_r r\left(\varepsilon+\dfrac{v^2}{2}\right)\right]}{\partial r}-\frac{\partial\left[\rho v_z\left(\varepsilon+\dfrac{v^2}{2}\right)\right]}{\partial z}\\ &\quad-\frac{1}{r}\frac{\partial(pv_r r)}{\partial r}-\frac{\partial(pv_z)}{\partial z}+\rho H.\end{aligned} \tag{3}$$

Here, Eq. (1) represents the mass conservation equation, Eq. (2) represents the ideal fluid momentum equation with the volume and viscous force terms neglected and Eq. (3) represents the energy equation. In these expressions, r is the spatial coordinate parallel to the surface of the target plate, z is the spatial coordinate perpendicular to the surface of the target plate, t is time, ρ, v_r, v_z and p are the density, velocity in the r direction, velocity in the z direction and pressure of the plasma, respectively, ε is the internal energy per unit mass, H is the net heat flux per unit mass, and the pressure is determined by the state equation $p=f(\rho,T)$, which relates to the density and temperature.[32]

2.2. Formulation of the self-similarity equation

In order to facilitate use of the results of analysis of the self-similar equation, we adopted convenient units shown in Table 1; the variables that have been normalized are specially marked with underscores in the formulae.

Table 1. Normalized values for scaled variables.

Time t (s)	Laser intensity I (10^{14} W·cm^{-2})	Wavelength λ (μm)	Ionic charge Z	Atomic mass A	Coulomb logarithm Λ
10^{-9}	1	1.06	65	240	5

The incident laser in this model is uniformly driven along the z direction (with a flat-top intensity distribution in the r direction) and has a flat-top intensity distribution in time. The energy deposition of this process is considered to be scalar deposition caused by inverse bremsstrahlung absorption, which is uniform and isotropic in all directions. Considering that the plasma expansion in the direction of laser incidence is uniform, it satisfies the form of a rarefaction wave solution that varies with time in this direction. Expansion in the r direction is symmetric, and the expansion velocities in these two directions are given by

$$v_r=\left(\frac{\mathrm{d}L_r/\mathrm{d}t}{L_r}\right)r=\alpha(t)r, \tag{4}$$

$$v_z=C_s+\frac{z}{t}. \tag{5}$$

Equation (4) indicates that the velocity is a linear function of each instantaneous position in time. L_r represent the plasma length in the r direction. $C_s=\sqrt{TZ/M_i}=T^{1/2}Z^{1/2}/M_i^{1/2}$

is the transient isothermal sound speed and $M_{\rm i}$ is the ion mass,[33,34] and the ionization degree formula of the corona region $Z = \frac{20}{3}[A(\mathrm{T/keV})]^{1/3}$ is used, where A is the atomic number of the considered element.

Combining the ideal gas law (pressure is proportional to the density of an ideal gas), we substitute the velocity expressions (4) and (5) into the momentum equation (Eq. (2)) and separate the variables in space and time, obtaining the following equations:

$$\rho(r) = c_1 \exp\left(-\frac{r^2}{2L_r^2}\right), \tag{6}$$

$$\rho(z) = c_2 \exp\left(-\frac{z}{L_z}\right), \tag{7}$$

where L_z represents the plasma length in the z direction. In order to derive the coefficient part of the above equations, the point of laser incidence on the target surface is defined in this paper as the origin of the coordinate system. m is the ablation mass per unit area of the target surface caused by the driving laser,[35] and the total ablation mass of the plasma generated in space is

$$\int_0^{\infty}\int_0^{L_r}\int_0^{2\pi} \rho(r)\rho(z) r\,\mathrm{d}r\,\mathrm{d}z\,\mathrm{d}\theta = m\pi L_0^2, \tag{8}$$

where L_0 represents the radius of the focal spot of the incident laser.

Therefore, the density description of the corona region has been obtained as

$$\rho = \frac{mL_0^2}{2L_zL_r^2}\exp\left(-\frac{r^2}{2L_r^2} - \frac{z}{L_z}\right). \tag{9}$$

Considering the premise of isothermal expansion and combining the mass conservation equation (1), momentum equation (2) and energy equation (3), the self-similar equations of two-dimensional fluid mechanics of a laser-irradiated slab target are derived as

$$C_{\rm s}L_z\left[\frac{2}{3}\frac{\mathrm{d}\ln T}{\mathrm{d}t} + \frac{1}{t}\right] = \frac{p}{\rho}, \tag{10}$$

$$L_r\frac{\mathrm{d}^2L_r}{\mathrm{d}t^2} = \frac{p}{\rho}, \tag{11}$$

$$C_v\frac{\mathrm{d}T}{\mathrm{d}t} = H - \frac{p}{\rho}\frac{(2\lambda+1)}{t}. \tag{12}$$

Here, C_v ($\equiv \mathrm{d}\varepsilon/\mathrm{d}T$) represents the specific heat per unit mass.

2.3. Equation of the ideal gas law

Upon the irradiation of a slab target by a flat-top laser of intensity I resulting in ablation, the relationship between plasma mass and time changes[36] is expressed as

$$\frac{\mathrm{d}m}{\mathrm{d}\underline{t}} = 1.7\times10^{-13}\frac{I^{2/3}}{(t\log\Lambda)^{1/3}}\left(\frac{A}{Z^{9/7}}\right)^{7/6}\left(\frac{Z}{Z+1}\right)^{7/6}. \tag{13}$$

Combining the ionization formula of the corona region $\underline{Z} = 4\times240^{1/3}[\underline{A}(\mathrm{T/keV})]^{1/3}/39$, and based on the convenient units in this paper and the integration of the mass ablation rate, the formula for the ablation mass that changes with time can be obtained as

$$\underline{m} = \frac{m}{10^{-4}} = \frac{28.833}{4-3\kappa}\frac{\underline{I}^{2/3}\underline{A}^{2/3}\underline{t}^{2/3}}{\underline{\Lambda}^{1/3}\underline{T}^{1/2}}. \tag{14}$$

The heating term of the laser is

$$H = \frac{I_0}{m}(1-\mathrm{e}^{-\tau_{\rm ib}}). \tag{15}$$

Here I is the total laser flux acting on the target and $\tau_{\rm ib}$ is the inverse bremsstrahlung absorption optical thickness of the thin foil

$$\tau_{\rm ib} = \int \kappa_{\rm ib}\,\mathrm{d}z. \tag{16}$$

The expression for the inverse bremsstrahlung absorption coefficient is

$$\kappa_{\rm ib} = \left(\frac{2}{\pi}\right)^{1/2}\frac{4}{3}\left[\frac{Ze^6(\log\Lambda)\lambda^2n_{\rm e}^2}{c^3(m_{\rm e}T)^{3/2}\left(1-\frac{n_{\rm e}}{n_{\rm c}}\right)^{1/2}}\right]. \tag{17}$$

Combining the definition of electronic density with the density Eq. (9) of the corona region, we obtain

$$n_{\rm e} = \frac{N_0Z\rho(r,z)}{A} = n_0\,\mathrm{e}^{-\frac{r^2}{2L_r^2}-\frac{z}{L_z}}. \tag{18}$$

Here $n_0 = \frac{N_0ZmL_0^2}{2AL_zL_r^2}$ represents the maximum electron density and $N_0 = 6.02\times10^{23}$ is the Avogadro constant.

In the model establishment stage above we analyzed that for the corona region, the plasma can be approximated as an ideal gas, and the state equations are given as

$$p = \frac{ZT\rho}{M_{\rm i}},\quad C_v = \frac{3}{2}\frac{Z}{M_{\rm i}}. \tag{19}$$

Combining these with the ionization formula, the state equations under the self-similar model are obtained as

$$p = \frac{20}{3[\mathrm{keV}]^{1/3}}\frac{A^{1/3}T^{4/3}\rho}{M_{\rm i}}, \tag{20}$$

$$C_v = \frac{10}{[\mathrm{keV}]^{1/3}}\frac{A^{1/3}T^{1/3}}{M_{\rm i}}. \tag{21}$$

3. Analysis and validation of the model

The process of interaction between the laser and the target is divided into two stages: the moment when the laser stops entering is the boundary point and the first stage is the interaction stage between the laser and the target, that is, $0 < t \le t_L$ (t_L represents the time when the laser stops heating), which is the stage we focus on. The second stage is after the laser stops entering, namely, the stop heating stage $t_L < t$.

3.1. The stage of interaction between the laser and the target

The process of evolution of the plasma in the corona region outside the critical density surface is of particular concern: the plasma that expands to this region has a density lower than the critical surface density. At this time, the inverse bremsstrahlung optical thickness $\tau_{\rm ib}$ decreases with time, and the heating rate also decreases with $\tau_{\rm ib}$. From Eq. (15), it can be obtained that at this time $H = \tau_{\rm ib} I_0/m$. Combining the density Eq. (18) and the inverse bremsstrahlung absorption coefficient Eq. (17) into the optical thickness Eq. (16), and integrating the entire plasma profile, the expression for optical thickness after integration can be obtained as

$$\tau_{\rm ib} = 0.017 \underline{m}^2 \underline{Z}^3 \underline{\lambda}^2 \underline{\Lambda A}^{-2} \underline{T}^{-3/2} L_z^{-1} \, {\rm e}^{-\frac{r^2}{L_r^2}}. \tag{22}$$

Combining Eqs. (20) and (21) with the ablation mass Eq. (14), and solving the similarity Eq. (12), the basic equation for temperature in this stage is obtained as

$$T = 3.812 \text{ keV } \underline{I}^{5/9} \underline{A}^{2/9} \underline{\lambda}^{2/3} \underline{\Lambda}^{2/9} \underline{t}^{2/9} \, {\rm e}^{-\frac{r^2}{3L_r^2}}. \tag{23}$$

By substituting Eq. (20) of the state into the self-similar equation in the r direction, and then combining it with Eq. (23), the basic equation for the length of the plasma in the r direction can obtained as

$$L_r \frac{{\rm d}^2 L_r}{{\rm d}\underline{t}^2} = 9.842 \times 10^{-4} \underline{I}^{20/27} \underline{\lambda}^{8/9} \underline{\Lambda}^{8/27} \underline{t}^{8/27} \underline{A}^{-10/27} \, {\rm e}^{-\frac{4r^2}{9L_r^2}}. \tag{24}$$

Further simplification yields the form of the solution for the length of the plasma in the r direction

$$L_r = 0.076 \underline{I}^{10/27} \underline{\lambda}^{4/9} \underline{\Lambda}^{4/27} \underline{A}^{-5/27} \, {\rm e}^{-\frac{2r^2}{9L_r^2}} \underline{t}^{31/27}. \tag{25}$$

Similarly, the basic equation for the length of the plasma in the z direction can be obtained as

$$L_z = 3.138 \times 10^{-2} \underline{I}^{10/27} \underline{\lambda}^{4/9} \underline{\Lambda}^{4/27} \underline{t}^{31/27} \underline{A}^{-5/27} \, {\rm e}^{-\frac{2r^2}{9L_r^2}}. \tag{26}$$

The equation for electronic density in space can also be obtained as

$$n_{\rm e} = 1.146 \times 10^{21} \underline{I}^{11/54} \underline{A}^{4/27} \underline{\lambda}^{-5/9} \underline{\Lambda}^{-14/27} \underline{t}^{-14/27} \, {\rm e}^{-\frac{2r^2}{9L_r^2} - \frac{z}{L_z}}. \tag{27}$$

3.2. The laser stop heating stage

For this stage, when the laser pulse stops, there is no further injection of laser energy and the mass of ablation will no longer change with time and become a constant. However, the ionization problem still exists, and the plasma continues to expand adiabatically in this stage. The result for the previous stage will serve as the initial condition for this stage, and the formula for analytical solution for this stage will be given based on this.

Commencing from the temperature equation and taking into account the initial conditions

$$T = T_L \underline{t}_L^{18/17} \underline{t}^{-18/17}. \tag{28}$$

Here T_L refers to the electron temperature at the end of laser irradiation.

The basic equations for the plasma length in the two directions of this stage are respectively

$$L_r = L_{rL} \underline{t}_L^{-5/17} \underline{t}^{5/17}, \tag{29}$$

$$L_z = L_{zL} \underline{t}_L^{-5/17} \underline{t}^{5/17}. \tag{30}$$

Through the definition of $n_{\rm e}$, the following equation can also be obtained:

$$n_{\rm e} = n_L \underline{t}_L^{21/17} \underline{t}^{-21/17}. \tag{31}$$

Here, L_{rL}, L_{zL} and n_L are, respectively, the plasma length and electronic density at the end of the previous stage when laser irradiation ceased.

3.3. Verification and discussion of the analytical solution

Based on the derivation process above, the length of the plasma after irradiation by a flat-top laser of intensity $I = 1 \times 10^{14}$ W·cm^{-2} and $\lambda = 1.06$ μm varies with time and space. The analytical solution for the plasma length is simplified using convenient units

$$L_r = 0.076 \, {\rm e}^{-\frac{2r^2}{9L_r^2}} \underline{t}^{31/27}. \tag{32}$$

To verify the correctness and reliability of the solution for the plasma length in the r direction, the results of Eq. (32) are compared with the solution of the basic equation (Eq. (24)) by plotting and analyzing (as shown in Fig. 2); by selecting different values of radial spatial position, the evolution of plasma length in the r direction with time is obtained. Firstly, it is found that when the radial position in space is constant, the density increases with time. Secondly, the solid line in the figure represents the result of the basic Eq. (24), and the dotted line represents the result of the solution Eq. (32). After comparison, it can be found that the trends of the solid line and the dotted line are in good agreement, and the error is extremely small, which proves that the solutions obtained with this model are accurate and reliable.

Figure 3 shows the variation of the plasma length in the r direction at four different moments ($t = 0.5$ ns, $t = 1.0$ ns, $t = 1.5$ ns and $t = 2.0$ ns). It is found that under the condition of fixed time, the length of the plasma in the r direction will decrease as r increases.

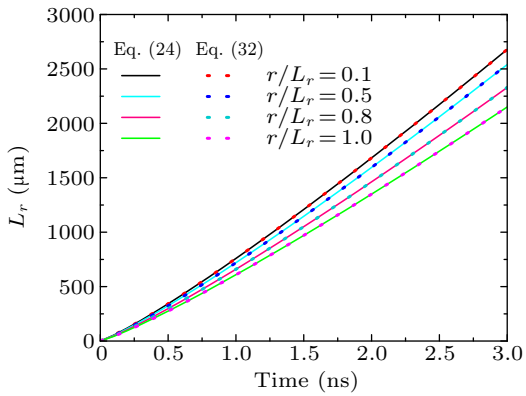


Fig. 2. Evolution of plasma length in the r direction with time.

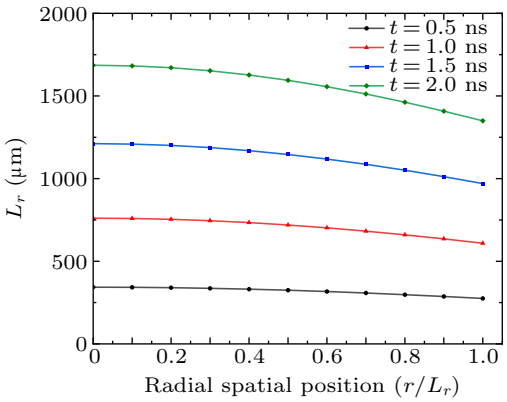


Fig. 3. The variation of plasma length in the r direction at four different moments ($t = 0.5$ ns, $t = 1.0$ ns, $t = 1.5$ ns and $t = 2.0$ ns).

In order to further verify the accuracy of the analytical results, the density analytical formula obtained in this paper was compared with the XRL2D program simulation image[27] under the same conditions (main laser intensity $I = 4.7 \times 10^{14}$ W·cm^{-2}, pre-pulse accounts for 3%, and a flat-top laser with a wavelength of 1.053 μm interacts with the Ag target). Figure 4(a) shows the XRL2D simulation image of Zheng and Zhang[27] and Fig. 4(b) shows an analytical image of the self-similar model. The comparison of the two images shows that the trends of simulation results and the analytical results are qualitatively consistent. Next, a more detailed quantitative comparative analysis is given. Figure 5 shows a comparison of axial density distribution between simulation and analysis, the blue dotted line is the XRL2D simulation result and the red dotted line is the analysis result. Figure 5 presents the density obtained from XRL2D simulations at an axial distance of 75 μm with a density of 2×10^{19} cm^{-3} and displays an analytically derived axial distance of 73 μm with a density of 2×10^{19} cm^{-3}. For the XRL2D simulation with a density of 1×10^{19} cm^{-3}, the axial distance is 110 μm while the corresponding analytical distance is 121 μm. Similarly, in the case of a simulation with a density of 2×10^{18} cm^{-3}, the axial distance is 270 μm, and the analytical distance is 258 μm, with an error fluctuation of less than 10%, further proving that the analytical model obtained in this paper is reliable.

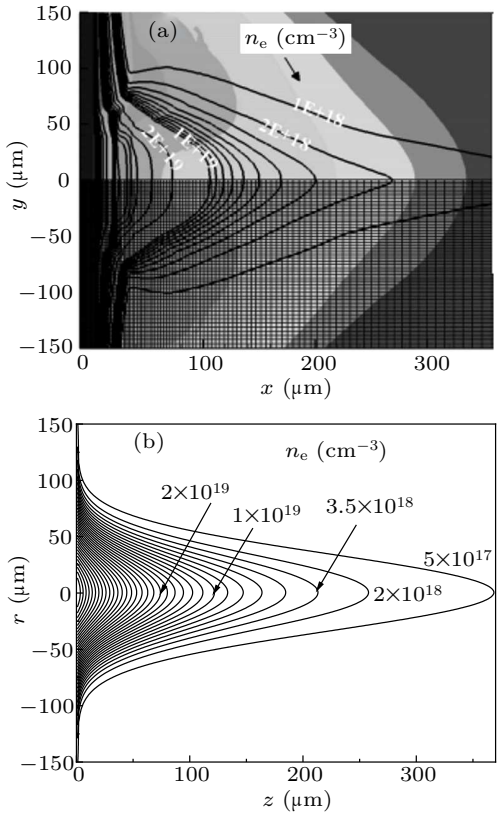


Fig. 4. Images of the plasma density distribution: (a) the XRL2D program simulation results[27] and (b) the self-similar model results.

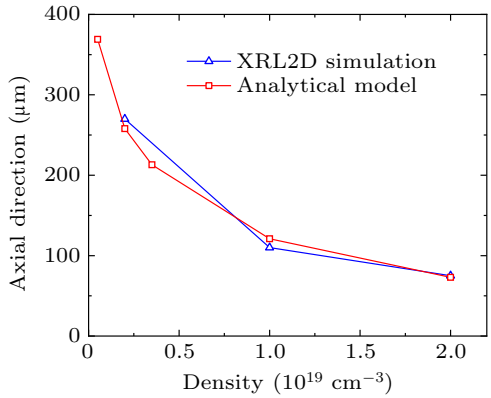


Fig. 5. Comparison of the distribution of density in the axial direction under simulation and analysis. The blue line is the simulation result, and the red line is the analytical result.

Figure 6 compares the temperature results of the XRL2D program simulation in Ref. [27] and the self-similar analytical results in this paper. As shown, the temperatures are symmetrically distributed when $r = 0$ μm, and the temperature reaches its maximum value when $r = 0$ μm. The trends of the results obtained with the self-similar model are roughly consistent with the results of XRL2D program simulation, showing a good match. Next, a more detailed quantitative comparative analysis is given. Figure 7 shows a comparison of the distribution of temperature in the axial direction under simulation and analysis, the blue line is the results of XRL2D simulation and the red line is the analytical result. From the comparison in Fig. 7, it can be seen that the analytical results are generally consistent in trend with the simulation results. It should

be noted that since the region near the slab target is a region of electron heat conduction with equal pressure and unequal temperature, the curves near the slab target in the program simulation result are concave. The model in this paper is based on isothermal conditions, so the analytical results are different from the results of XRL2D program simulation in the region near the target; the region where the temperature curve near the target concaves inward in the simulation results is not considered in our model.

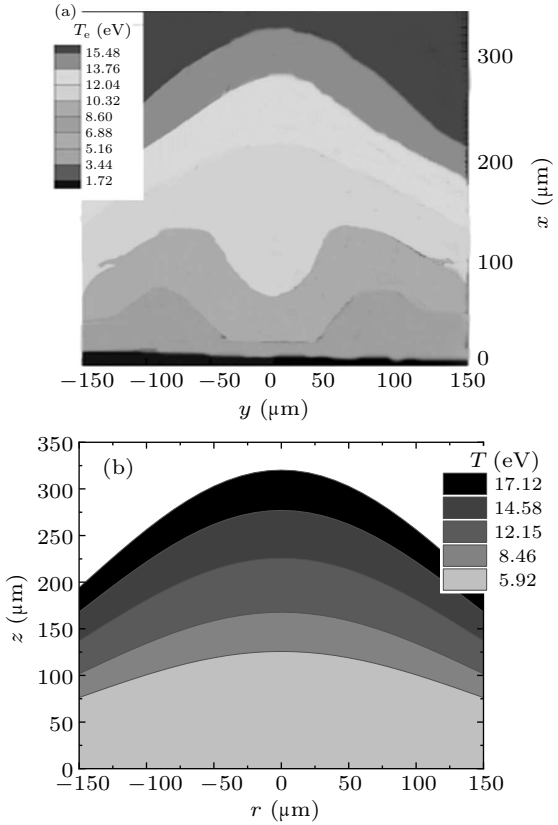


Fig. 6. Two-dimensional spatial distribution of temperature: (a) XRL2D program simulation results and (b) self-similar model results.

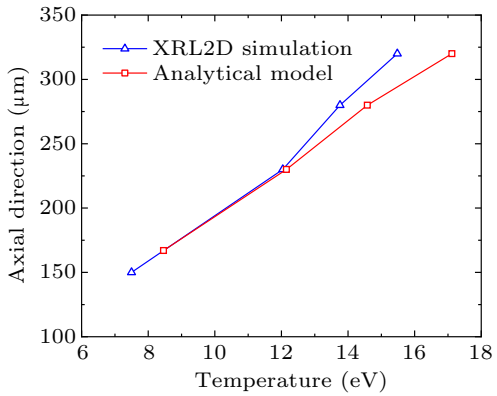


Fig. 7. Comparison of the distribution of temperature in the axial direction under simulation and analysis, the blue line is the simulation result and the red line is the analytical result.

Combining the convenient units for the laser conditions in Table 1 ($I = 1 \times 10^{14}$ W·cm^{-2}, $\lambda = 1.06$ μm) and the analytical formula for electron density, Fig. 8 shows the spatial distribution of plasma electron density at different times. The evolution of electron density in both directions shows that at the beginning of the interaction between the laser pulse and the target, the plasma begins to generate and expands outward with time. With increasing time, the plasma expands outward in a nearly regular circular shape and this radial expansion is accompanied by axial expansion in the reverse light path. As the laser continuously interacts with the target plasma, the plasma temperature continues to rise, the movement speed accelerates and the plasma expansion becomes more and more intense; moreover, the distribution of plasma density in the entire region is uneven. The greater the distance from the target surface, the lower the density of the plasma. This is because the laser cannot enter the region inside the critical density surface, the density of the plasma that expands outside gradually decreases and the electron density will become increasingly sparse.

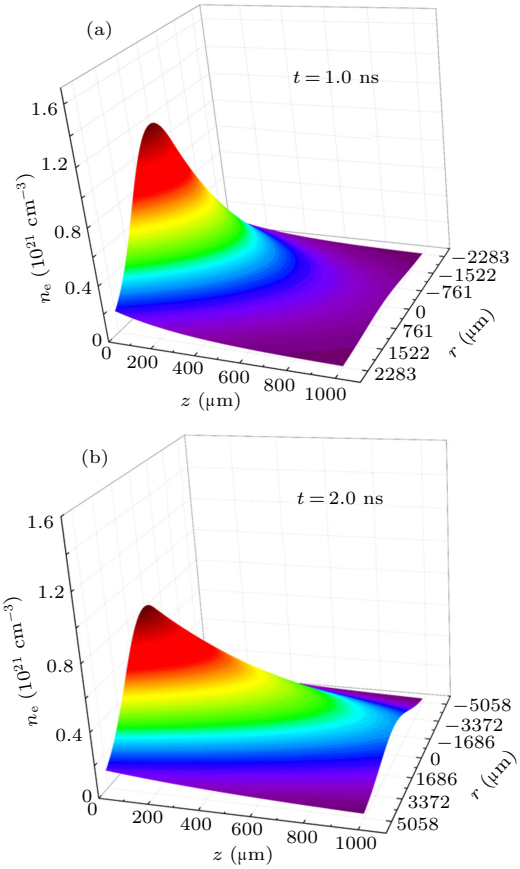


Fig. 8. Spatial distribution diagram of plasma electron density: (a) $t =$ 1.0 ns, (b) $t = 2.0$ ns.

For the fixed time $t = 1.0$ ns, Fig. 9(a) shows the evolution of electron density with radial spatial position (r direction). It can be observed that the electron density is symmetrically distributed with the target point as the center, and the electron density is maximum at $r = 0$ μm. With increase in the spatial position, the electron density gradually decreases. Figure 9(b) shows that the electron density along the axial direction (z direction) is approximately exponentially distributed,

and the density decreases with increase in the spatial position; the decay rate gradually decreases.

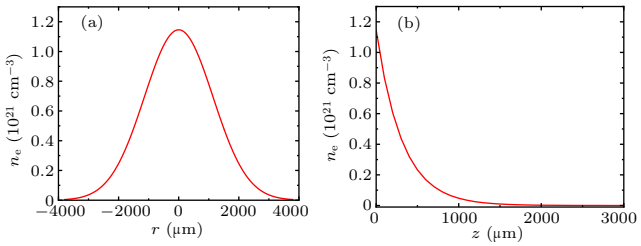


Fig. 9. The relationship between plasma electron density and spatial position (a) for the radial direction (r direction) and (b) for the axial direction (z direction).

Figure 10 shows the spatial distribution of plasma electron temperature at two different times. For a fixed time, the electron temperature generated at the target point is the highest, and the temperature decreases exponentially with increase in the spatial position with the target point as the center. By comparing the electron temperature at different times, it can be found that with continuous incidence of the laser the electron temperature also increases significantly.

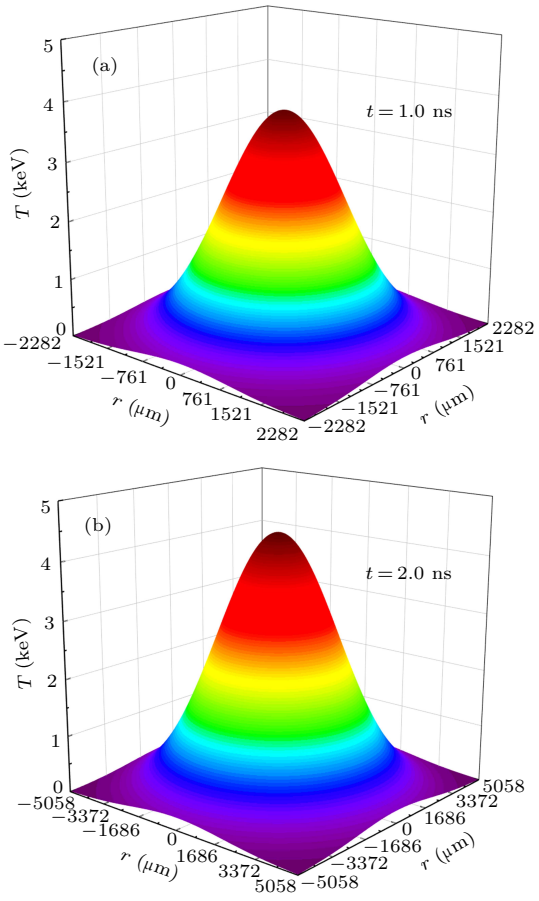


Fig. 10. The relationship between plasma electron temperature and spatial position: (a) $t = 1.0$ ns, (b) $t = 2.0$ ns.

For laser interaction experiments, it is desirable to maximize the absorption and utilization of laser energy by the plasma, providing the initial energy for subsequent experimental stages. In the three regions produced by laser irradiation of the solid target, since the laser cannot penetrate beyond the critical density surface, energy absorption mainly occurs in the corona region outside the critical density surface. Energy is then transferred to the conduction region through electron thermal conduction, leading to heating in that region. The more laser energy that is absorbed in the corona region, the more energy the electrons generated by laser irradiation on the solid target will acquire, resulting in higher electron temperatures.

Figure 11 shows the relationship between temperature, pulse duration and spatial position for four different laser intensities. As the laser intensity increases, the temperature distribution in space significantly increases. For instance, when the laser intensity increases from 0.5×10^{14} W·cm^{-2} (Fig. 9(a)) to 5.0×10^{14} W·cm^{-2} (Fig. 11(d)), the maximum temperature in space rises from 3.3 keV to 11.9 keV and the temperature increases by about 2.6 times. Initially, the temperature rises rapidly with time upon laser irradiation; however, during the later stages of laser–plasma interaction, the rate of growth of electron temperature slows, suggesting that in order to achieve the same temperature shorter pulse durations are required for higher laser intensities. For example, at the same spatial position (considering the highest temperature point in space), achieving a temperature of 3 keV requires a pulse duration of 1.93 ns for a laser intensity of 0.5×10^{14} W·cm^{-2}, 0.34 ns for 1.0×10^{14} W·cm^{-2}, 0.17 ns for 2.0×10^{14} W·cm^{-2} and only 0.068 ns for 5.0×10^{14} W·cm^{-2}, compared with the 1.93 ns required for 0.5×10^{14} W·cm^{-2}; the pulse duration is nearly 28 times shorter for 5.0×10^{14} W·cm^{-2}.

In summary, both increasing the laser intensity and extending the pulse duration can achieve temperature enhancement. However, prolonging the pulse duration is relatively easier in laser experiments.

From the earlier discussion in this paper, we know that both temperature gradients and density gradients vary with changes in pulse duration; in the field of high-energy-density physics, these gradients have a significant impact on phenomena such as magnetic field generation and x-ray production. The Biermann effect tells us that the strength of self-generated magnetic fields primarily depends on the gradients of density and temperature, with larger gradients leading to stronger self-generated magnetic fields.[9] Additionally, experimental theories related to x-ray generation indicate that smoother density gradients favor x-ray propagation.[22]

Figure 12(a) shows the evolution of temperature with spatial position and pulse duration. From the evolutionary relationship with spatial position, it is found that closer to the laser focal point the temperature gradient is smaller, as the spatial position increases the temperature gradient first increases, then decreases and finally gradually flattens out. Taking the example of a laser intensity of 1.0×10^{14} W·cm^{-2} and a pulse

duration of 1 ns, we calculated the temperature gradients at various spatial positions: 76–304 μm, 608–836 μm, 1140–1368 μm and 1748–1976 μm. The results show that the temperature gradient is smallest (0.62) near the target point at 76–304 μm, while it reaches its maximum value (1.80) at 608–836 μm. With the increase in spatial position to the range of 1140–1368 μm, the gradient decreases to 1.67 and continues to decrease. These findings align perfectly with previous experimental and simulation studies, which found that annular magnetic fields are mainly generated at the edge of plasma bubbles.[9]

Figure 12(b) shows that at the same spatial position, the temperature gradient varies with different pulse durations. As the pulse duration increases from 0.5 ns to 3 ns, the maximum temperature gradient also increases from 1.52 to 2.27, indicating that when the other conditions remain consistent, regulating the duration of the laser is a very effective means to changing the temperature gradient.

To explore the impact of changes in laser intensity on the temperature gradient, the relationship between temperature and spatial position and the evolution of the laser intensity is given in Fig. 13. Here the laser pulse duration is fixed at 3 ns. From Fig. 13(a), it is found that increasing the laser intensity effectively raises the temperature; this enhancement occurs because the increase in laser intensity leads to a corresponding increase in the energy incident in the target, and the energy obtained by the plasma and electrons is also increased. Observing Fig. 13(b), at the selected spatial position of 2148–2685 μm, under different laser intensities, the temperature gradient varies significantly, as the laser intensity increases from 0.5×10^{14} W·cm^{-2} to 5.0×10^{14} W·cm^{-2}, the temperature gradient increases from 1.54 to 5.55; this highlights the substantial impact of regulating laser intensity on the temperature gradient while keeping other conditions constant.

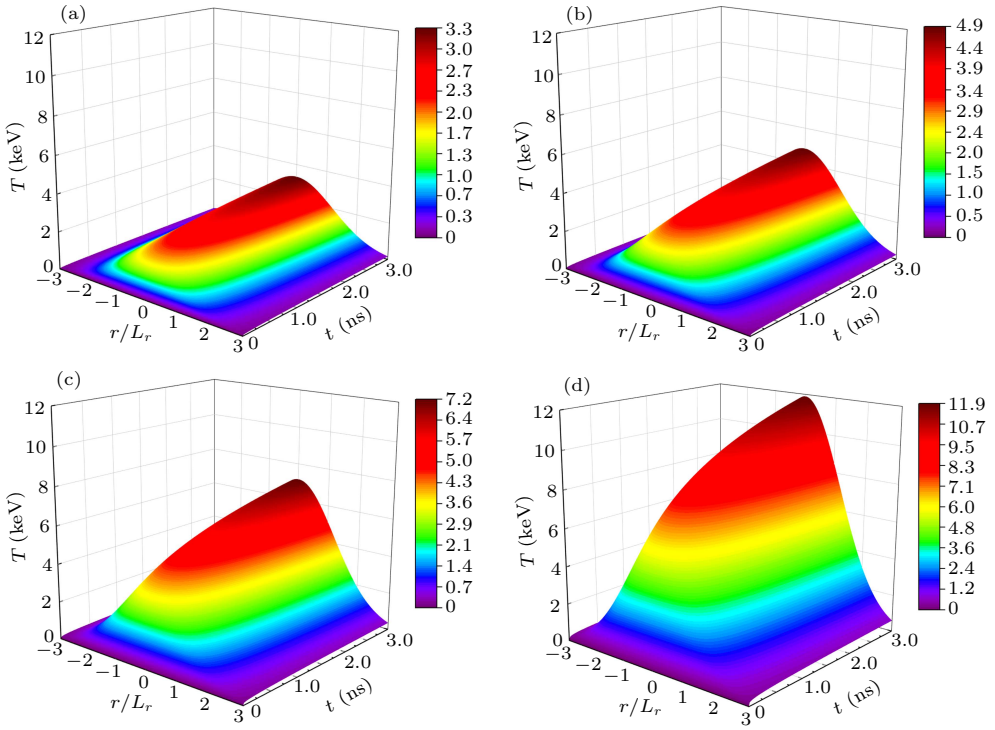


Fig. 11. The evolution of temperature with spatial position and pulse duration under different laser intensities: (a) $I = 0.5 \times 1014$ W·cm^{-2}, (b) $I = 1.0 \times 10^{14}$ W·cm^{-2}, (c) $I = 2.0 \times 10^{14}$ W·cm^{-2} and (d) $I = 5.0 \times 10^{14}$ W·cm^{-2}.

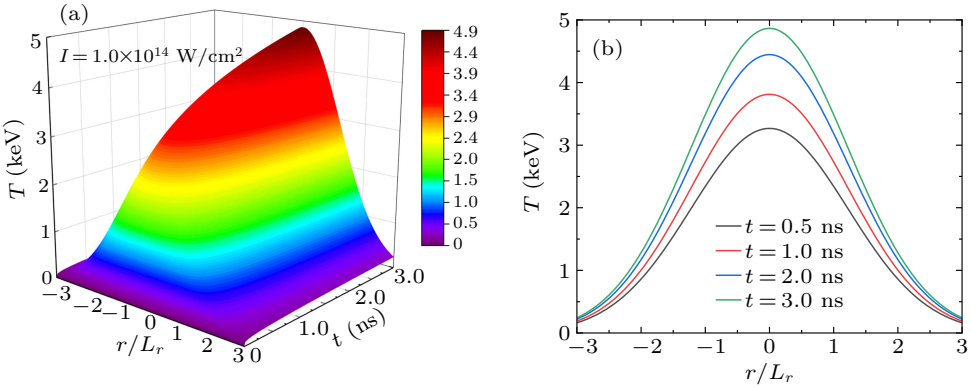


Fig. 12. (a) The evolution of temperature with spatial position and pulse duration. (b) The relationship of temperature with spatial position for different pulse durations.

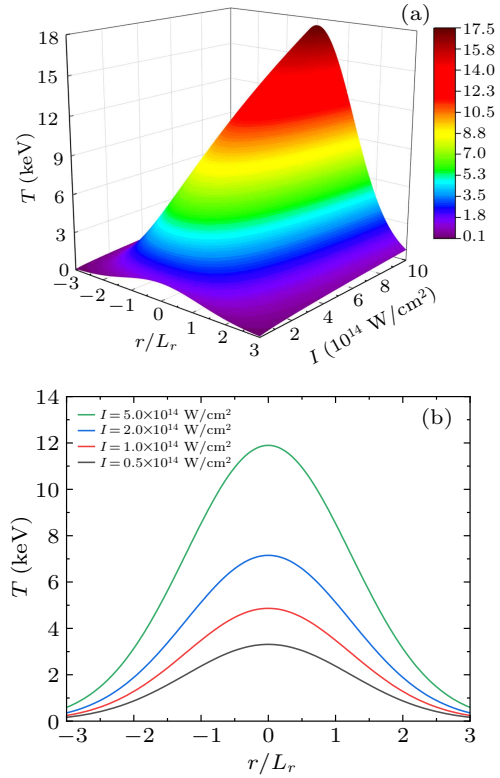


Fig. 13. (a) The evolution of temperature with spatial position and pulse duration. (b) The relationship between temperature and spatial position under different laser intensities.

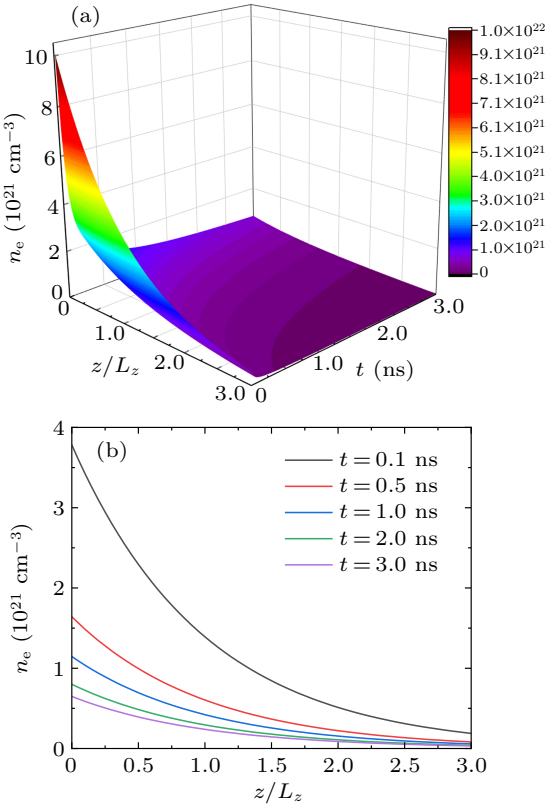


Fig. 14. (a) The evolution of density with spatial position and pulse duration. (b) The relationship between density and spatial position for different pulse durations.

Figure 14(a) depicts the evolution of density with spatial position and pulse duration. From the relationship between spatial position and density we can see that as spatial position increases the density gradient gradually decreases. Let us consider a laser intensity of 1.0×10^{14} W·cm^{-2} and a pulse duration of 1 ns. We calculated the density gradient at various spatial positions: 76–304 μm, 608–836 μm, 1140–1368 μm and 1748–1976 μm. The statistical results reveal that the density gradient is highest near the target point at 76–304 μm, reaching 8.95×10^{20} at 608–836 μm. The density gradient decreases by half to 4.44×10^{20} as the spatial position increases to the range of 1748–1976 μm, then the gradient further reduces to 0.99×10^{20}. Clearly, spatial position has a significant influence on the density gradient. Observing Fig. 14(b), the density gradient decreases with increasing laser pulse duration. Focusing on the spatial position near the target point, statistical calculations show that as the pulse duration increases from 0.1 ns to 3 ns, the density gradient decreases from 2.95×10^{21} to 0.51×10^{21}. This indicates that while other conditions are kept constant, adjusting the laser's duration is an effective means to alter the density gradient.

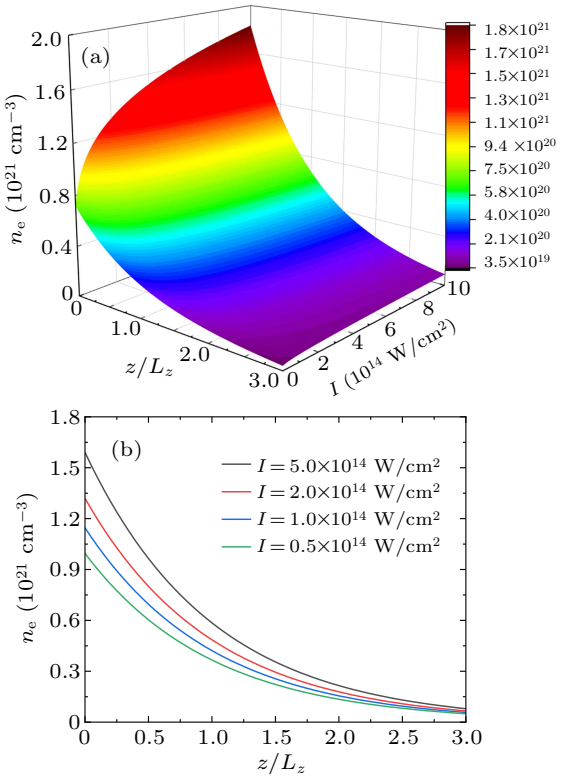


Fig. 15. (a) The evolution of density with spatial position and laser intensity. (b) The relationship between density with spatial position for different laser intensities.

To investigate the impact of variations in laser intensity on the density gradient, Fig. 15 shows the evolution of density with spatial position and with laser intensity, Here, the laser pulse duration is fixed at 1 ns. From Fig. 15(a), it is found that increasing laser intensity effectively enhances the density within the spatial domain. Observing Fig. 15(b) and selecting the spatial position range of 608–836 μm, for different incident laser intensities the density gradient is also different. As the laser intensity increases from 0.5×10^{14} W·cm^{-2}

to 5.0×10^{14} W·cm^{-2}, the density gradient increases from 3.86×10^{20} to 6.17×10^{20}.

Regarding the impact on density gradient, adjusting the laser intensity and the pulse duration are both effective strategies. However, when comparing the trends in Figs. 14(b) and 15(b), it becomes evident that altering the pulse duration is more efficient for modifying the density gradient.

In summary, it has been observed that changes in temperature gradient and density gradient are influenced differently by laser intensity and pulse duration. The temperature gradient increases with longer pulse duration and higher laser intensity; as the spatial position increases, the farther away from the target point the temperature gradient first increases and then decreases. On the other hand, the behavior of the density gradient differs from that of the temperature gradient: as the direction from the target point increases, the density gradient gradually decreases as the spatial position increases. Moreover, as the pulse duration increases, the density gradient decreases, but gradually increases as the laser intensity increases.

4. Conclusion

This paper aims to study the specific evolution of physical quantities such as the electron density, electron temperature and plasma length in the corona region during the interaction between laser and target in a quasi-three-dimensional model that is more closely related to real experiments. The purpose of this study was to obtain the relevant analytical formulae for these key physical parameters and to obtain the analytical formulae (23)–(31). The results obtained by comparing the analytical results with the results of expensive and time-consuming numerical simulations show a very consistent trend. On this basis, three-dimensional spatial distribution diagrams of electron density and electron temperature are provided using the analytical formulae of the model (see Figs. 8 and 10). It is worth noting that the quasi-three-dimensional analytical model of the interaction between a point-focused laser and a slab target has rarely been mentioned in previous work. The self-similar model established in this paper has irreplaceable advantages, such as a clear process description, an intuitive scaling relationship and efficient calculation compared with the complicated and time-consuming numerical simulation.

Acknowledgements

Project supported by the Strategic Priority Research Program of the Chinese Academy of Sciences (Grant No. XDA25051000) and the National Natural Science Foundation of China (Grant No. 11574390).

References

[1] Li C K, Séguin F H, Frenje J A, Rygg J R, Petrasso R D, Town R P J, Amendt P A, Hatchett S P, Landen O L, Mackinnon A J, Patel P K, Smalyuk V A, Sangster T C and Knauer J P 2006 *Phys. Rev. Lett.* **97** 135003

[2] Li C K, Séguin F H, Frenje J A, Rygg J R, Petrasso R D, Town R P J, Landen O L, Knauer J P and Smalyuk V A 2007 *Phys. Rev. Lett.* **99** 055001

[3] Yates M A, Van Hulsteyn D B, Rutkowski H, Kyrala G and Brackbill J U 1982 *Phys. Rev. Lett.* **49** 1702

[4] Zhong J Y, Li Y T, Wang X G, Wang J Q, Dong Q L, Xiao C J, Wang S J, Liu X, Zhang L, An L, Wang F L, Zhu J Q, Gu Y, He X T, Zhao G and Zhang J 2010 *Nat. Phys.* **6** 984

[5] Zhong J Y, Lin J and Li Y T, *et al*. 2016 *Astrophys. J. Suppl. Ser.* **225** 30

[6] Lebedev S V, Frank A and Ryutov D D 2019 *Rev. Mod. Phys.* **91** 025002

[7] Takabe H and Kuramitsu Y 2021 *High Power Laser Sci. Eng.* **9** e49

[8] Fiksel G, Fox W, Bhattacharjee A, Barnak D H, Chang P Y, Germaschewski K, Hu S X and Nilson P M 2014 *Phys. Rev. Lett.* **113** 105003

[9] Zhong J Y, Yuan X X, Han B, Sun W and Ping Y L 2018 *High Power Laser Sci. Eng.* **6** e48

[10] Kodama R, Norreys P A, Mima K, *et al*. 2001 *Nature* **412** 798

[11] Wilks S C, Kruer W L, Tabak M and Langdon A B 1992 *Phys. Rev. Lett.* **69** 1383

[12] Borghesi M, Fuchs J, Bulanov S V, MacKinnon A J, Patel P K and Roth M 2006 *Fusion Sci. Technol.* **49** 412

[13] Liu Z D, Zhong J Y, Yuan X H, *et al*. 2023 *Chin. Phys. B* **32** 110702

[14] Zylstra A B, Hurricane O A, Callahan D A, *et al*. 2022 *Nature* **601** 542

[15] Abu-Shawareb H, Acree R, Adams P, *et al*. 2022 *Phys. Rev. Lett.* **129** 075001

[16] Hu S X, Ceurvorst L, Peebles J L, *et al*. 2023 *Phys. Rev. E* **108** 035209

[17] Zhang C L, Zhang Y H, Yuan X H, *et al*. 2024 *Chin. Phys. B* **33** 025201

[18] Bel'kov S A, Bondarenko S V, Demchenko N N, Garanin S G, Gus'kov S Y, Kuchugov P A, Rozanov V B, Stepanov R V, Yakhin R A and Zmitrenko N V 2019 *Plasma Phys. Control. Fusion* **61** 025011

[19] Niemann C, Divol L, Froula D H, Gregori G, Jones O, Kirkwood R K, MacKinnon A J, Meezan N B, Moody J D, Sorce C, Suter L J, Bahr R, Seka W and Glenzer S H 2005 *Phys. Rev. Lett.* **94** 085005

[20] Stevenson R M, Suter L J, Oades K, Kruer W, Slark G E, Fournier K B, Meezan N, Kauffman R, Miller M, Glenzer S, Niemann C, Grun J, Davis J, Back C and Thomas B 2004 *Phys. Plasmas* **11** 2709

[21] Li Y J and Zhang J 2001 *Phys. Rev. E* **63** 036410

[22] Li Y J, Lu X and Zhang J 2002 *Phys. Rev. E* **66** 046501

[23] Cheng T, Li Y J, Meng L M and Zhang J 2008 *Europhys. Lett.* **84** 45001

[24] London R A and Rosen M D 1986 *Phys. Fluids* **29** 3813

[25] Chen D, Cai D F and Su H S 2023 *Chin. Phys. B* **32** 098903

[26] Chen M Z, Wang L Y, Liu G, Ge C Q, Li D C and Liang Q X 2023 *Chin. Phys. B* **32** 048103

[27] Zheng W D and Zhang G P 2007 *Chin. Phys.* **16** 2439

[28] Zhang Z R and Huang J P 2022 *Chin. Phys. Lett.* **39** 075201

[29] Liu Y X, Zhang Q Z, Zhao K, Zhang Y R, Gao F, Song Y H and Wang Y N 2022 *Chin. Phys. B* **31** 085202

[30] Sanz J, Garnier J, Cherfils C, Canaud B, Masse L and Temporal M 2005 *Phys. Plasmas* **12** 112702

[31] Zhu Z Y, Liu Y X, Li Y J and Zhang J 2022 *Chin. Phys. B* **31** 105202

[32] Remington B A, Drake R P and Ryutov D D 2006 *Rev. Mod. Phys.* **78** 755

[33] Colombant D and Tonon G F 1973 *J. Appl. Phys.* **44** 3524

[34] Bobin J L, Colombant D and Tonon G 1972 *Nucl. Fusion* **12** 445

[35] Sigel R, Tsakiris G D, Lavarenne F, *et al*. 1990 *Phys. Rev. Lett.* **65** 587

[36] De Groot J S, Estabrook K G, Kruer W L, Drake R P, Mizuno K and Cameron S M 1992 *Phys. Fluids B* **4** 701